A Network of Phosphatidylinositol 4,5-bisphosphate Binding Sites Regulate Gating of the Ca^{2+}-activated Cl^- Channel ANO1 (TMEM16A)

Kuai Yu [a,2], Tao Jiang [b,2], YuanYuan Cui [a], Emad Tajkhorshid [b,1] and H. Criss Hartzell [a,1]

[a] *Department of Cell Biology, Emory University School of Medicine, Atlanta, GA, USA*
[b] *NIH Center for Macromolecular Modeling and Bioinformatics, Beckman Institute for Advanced Science and Technology, Department of Biochemistry, and Center for Biophysics and Quantitative Biology, University of Illinois at Urbana-Champaign, Urbana, IL, USA*

[1] **Corresponding authors:**
H. Criss Hartzell, Department of Cell Biology, 535 Whitehead Biomedical Research Building, 615 Michael St., Emory University School of Medicine, Atlanta, GA 30322 USA
Phone: 404-242-5719; email: criss.hartzell@emory.edu.

Emad Tajkhorshid, NIH center for Macromolecular Modeling and Bioinformatics, Department of Biochemistry, Center for Biophysics and Quantitative Biology, University of Illinois at Urbana-Champaign, Urbana, IL 61801 USA
Phone: 217-244-6914; email: tajkhors@illinois.edu

[2] Kuai Yu and Tao Jiang contributed equally to this work.

Keywords:
chloride channel, protein-lipid interaction, phospholipid, structure-function, molecular dynamics

Abstract

ANO1 (TMEM16A) is a Ca^{2+}-activated Cl^- channel that regulates diverse cellular functions including fluid secretion, neuronal excitability, and smooth muscle contraction. ANO1 is activated by elevation of cytosolic Ca^{2+} and modulated by phosphatidylinositol 4,5-bisphosphate ($PI(4,5)P_2$). Here we describe a closely concerted experimental and computational study, including electrophysiology, mutagenesis, functional assays, and extended sampling of lipid-protein interactions with molecular dynamics (MD) to characterize $PI(4,5)P_2$ binding modes and sites on ANO1. ANO1 currents in excised inside-out patches activated by 270 nM Ca^{2+} at +100 mV are increased by exogenous $PI(4,5)P_2$ with an EC_{50} = 1.24 μM. The effect of $PI(4,5)P_2$ is dependent on membrane voltage and Ca^{2+} and is explained by a stabilization of the ANO1 Ca^{2+}-bound open state. Unbiased atomistic MD simulations with 1.4 mol% $PI(4,5)P_2$ in a phosphatidylcholine bilayer identified 8 binding sites with significant probability of binding $PI(4,5)P_2$. Three of these sites captured 85% of all ANO1 - $PI(4,5)P_2$ interactions. Mutagenesis of basic amino acids near the membrane-cytosol interface found three regions of ANO1 critical for $PI(4,5)P_2$ regulation that correspond to the same three sites identified by MD. $PI(4,5)P_2$ is stabilized by hydrogen bonding between amino acid sidechains and phosphate/hydroxyl groups on $PI(4,5)P_2$. Binding of $PI(4,5)P_2$ alters the position of the cytoplasmic extension of TM6, which plays a crucial role in ANO1 channel gating, and increases the accessibility of the inner vestibule to Cl^- ions. We propose a model consisting of a network of three $PI(4,5)P_2$ binding sites at the cytoplasmic face of the membrane allosterically regulating ANO1 channel gating.

Significance statement

Membrane proteins dwell in a sea of phospholipids that not only structurally stabilize the proteins by providing a hydrophobic environment for their transmembrane segments, but also dynamically regulate protein function. While many cation channels are known to be regulated by phosphatidylinositol 4,5-bisphosphate ($PI(4,5)P_2$), relatively little is known about anion channel regulation by phosphoinositides. Using a combination of patch clamp electrophysiology and atomistic molecular dynamics simulations, we have identified several $PI(4,5)P_2$ binding sites in ANO1 (TMEM16A), a Cl^- channel that performs myriad physiological functions from epithelial fluid secretion to regulation of electrical excitability. These binding sites form a band at the cytosolic interface of the membrane that we propose constitute a network to dynamically regulate this highly allosteric protein.

Introduction

Ca^{2+}-activated Cl^- channels (CaCCs) are jacks of all trades and masters of many. These ion channels facilitate the passive flow of Cl^- across cell membranes in response to elevation of cytosolic Ca^{2+} (1). Although CaCCs are probably best known for driving fluid secretion across mammalian epithelia, they are intimately involved in manifold physiological functions in all eukaryotes. CaCCs mediate action potentials in algae, the fast block to polyspermy in Anuran eggs, and regulate functions as diverse as smooth muscle contraction, nociception, neuronal excitability, insulin secretion, and cell proliferation and migration in mammals (1-13). While there are several types of CaCCs, the so-called classical CaCCs are encoded by the *ANO1* (*TMEM16A*) and *ANO2* (*TMEM16B*) genes (14-16).

Activation of ANO1 in its physiological context typically begins with ligand binding to a G-protein coupled receptor that activates phospholipase-C (PLC) (17-20). PLC hydrolyzes phosphatidylinositol 4,5-bisphosphate ($PI(4,5)P_2$) in the plasma membrane to produce diacylgycerol and inositol 1,4,5-trisphosphate ($Ins(1,4,5)P_3$). $Ins(1,4,5)P_3$ binding to $Ins(1,4,5)P_3$ receptors then triggers release of Ca^{2+} from internal ER stores and initiates store-operated Ca^{2+} entry. The resulting rise in cytosolic Ca^{2+} activates Cl^- flux because of conformational changes induced by direct binding of Ca^{2+} to the ANO1 protein (21-25). Calmodulin is not required for channel activation (21, 26).

Structurally, ANO1 is a dimer with each subunit composed of 10 transmembrane **(TM)** segments. The Cl^- selective pore of each subunit is surrounded by TMs 4–7 (22, 23, 27, 28) and each subunit has a Ca^{2+} binding site formed by amino acids E654, E702, E705, E734, and D738 in TMs 6–8 (22-25, 29). Channel gating involves conformational changes of TM6 (24, 25, 30).

ANO1 is also regulated by $PI(4,5)P_2$ (31-35). Ta et al. (33) have reported that $PI(4,5)P_2$ stimulates ANO1 currents in excised patches. We (32) and Tembo et al. (35) have shown that $PI(4,5)P_2$ can prevent and rescue Ca^{2+}-dependent rundown caused by spontaneous $PI(4,5)P_2$ hydrolysis. In whole-cell recording, we also showed that reduction of cellular $PI(4,5)P_2$ by the voltage sensitive phosphatase Dr-VSP or by activation of GPCRs causes a reduction in ANO1 current (32). Pritchard et al. (34) show biochemical evidence that $PI(4,5)P_2$ binds to ANO1, but they report that exogenous $PI(4,5)P_2$ decreases endogenous Cl^- currents thought to be encoded by *ANO1* in inside-out patches of pulmonary artery cells, in contrast to the results with heterologously-expressed ANO1 (32, 33).

$PI(4,5)P_2$ binding sites typically have two or more positively charged amino acids with at least one Lys, and at least one aromatic residue (36-38). One well-known $PI(4,5)P_2$ binding site is the pleckstrin homology (PH) domain which binds $PI(4,5)P_2$ in a pocket of basic amino acids that are non-contiguous in the primary sequence but are close in proximity in the folded protein (39). On the other hand, "electrostatic type" binding sites typified by the CALM domain are clusters of contiguous basic amino acids that interact with phospholipids relatively non-specifically without forming a binding pocket (40). A wide variety of ion channels are regulated by $PI(4,5)P_2$ (36-38, 41). In K_{ir} channels, these basic amino acids are located near the interface between the cytosol and the bulk lipid bilayer where the polar headgroups of lipids typically reside (42-44).

The objective of this study was to understand the mechanisms of regulation of ANO1 by $PI(4,5)P_2$ and identify amino acids that stabilize $PI(4,5)P_2$ binding. We find that $PI(4,5)P_2$ stimulates ANO1 currents in excised patches in a voltage- and Ca^{2+}- regulated manner. Mutagenesis and molecular dynamics (MD) simulations reveal that ANO1 has multiple $PI(4,5)P_2$ binding sites. These data add to a growing body of knowledge showing that ANO1 is a highly allosteric protein that is gated by a network of interactions involving both Ca^{2+} and $PI(4,5)P_2$.

Results

$PI(4,5)P_2$ is a Positive Regulator of ANO1 Currents.

To determine the effect of $PI(4,5)P_2$ on ANO1, we transiently expressed ANO1 in HEK293 cells and measured the effect of dioctanoyl phosphatidylinositol 4,5-bisphosphate (diC8-$PI(4,5)P_2$), a water-soluble, short acyl chain $PI(4,5)P_2$, on inside-out excised patches. To reduce variability caused by different amounts of endogenous $PI(4,5)P_2$, we first removed $PI(4,5)P_2$ from the membrane patch by excising it into a solution containing 10 mM Mg^{2+} and 0 Ca^{2+}/5 mM EGTA. Mg^{2+} competes with ANO1 for binding to $PI(4,5)P_2$ by electrostatically masking negative charges on $PI(4,5)P_2$ (45). ANO1 currents were measured during voltage steps first in the presence of 270 nM Ca^{2+} ($I_{initial}$) and then with 270 nM Ca^{2+} plus 10 μM diC8-$PI(4,5)P_2$ (I_{PIP2}) (Fig. 1A). The increase in current (ΔI_{PIP2}) was calculated as ($I_{PIP2}/I_{initial}$-1)*100%. On average, application of diC8-$PI(4,5)P_2$ at +100 mV increased the current 79.1 ± 15.1% (n = 8). The effect of diC8-$PI(4,5)P_2$ was slowly reversible: the currents decreased in amplitude when the patch was exposed to 270 nM Ca^{2+} in the absence of diC8-$PI(4,5)P_2$ and exposure

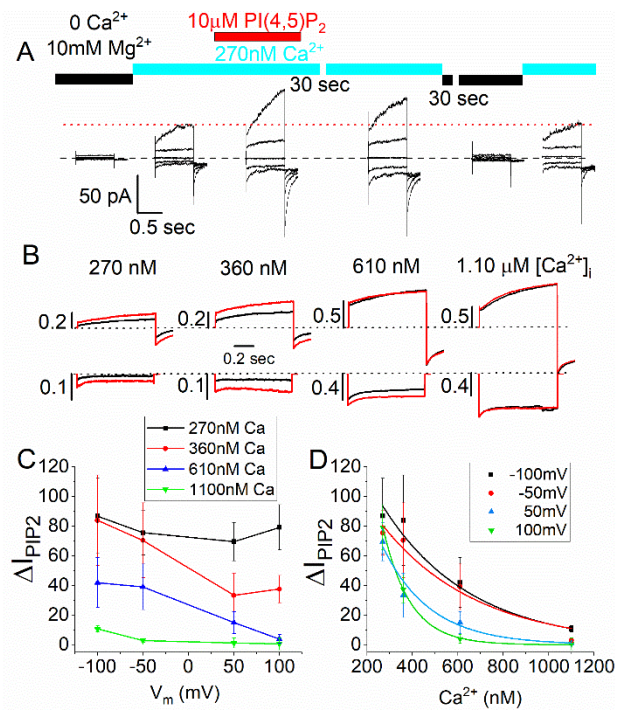

Figure 1. $PI(4,5)P_2$ stimulates ANO1 current. **(A)** Current traces from a single inside-out excised patch exposed sequentially to solutions indicated above each set of traces. Each set of traces was obtained by voltage pulses from a holding potential of 0 mV to -100 mV, -50 mV, 0 mV, 50 mV, and 100 mV. **(B)** Representative current traces from different patches exposed to different Ca^{2+} concentrations. Black trace: control solution without $PI(4,5)P_2$. Red trace: same solution with added 10 μM diC8-$PI(4,5)P_2$. Top row: +100 mV. Bottom row: -100 mV. Scale bars represent current amplitudes normalized to the current obtained from the same patch exposed to 20 μM Ca^{2+} to evoke a maximal current. **(C)** Voltage-dependence of $PI(4,5)P_2$ stimulation of ANO1 current. Percent change in current amplitude caused by 10 μM diC8-$PI(4,5)P_2$ (ΔI_{PIP2}) is plotted vs. voltage for patches exposed to 270 nM (black squares), 360 nM (red circles), 610 nM (blue triangles), or 1.1 μM (green inverted triangles) free Ca^{2+}. **(D)** Effect of free Ca^{2+} on stimulation of ANO1 current by diC8-$PI(4,5)P_2$. Percent change in current amplitude is plotted vs. free Ca^{2+} concentration at -100 mV (black squares), -50 mV (red circles), 50 mV (blue triangle), 100 mV (green inverted triangle).

to 10 mM Mg^{2+} reduced the current further to its initial level (Fig. 1A).

The Effect of PI(4,5)P_2 is Regulated by Voltage and Ca^{2+}.

The effect of diC8-PI(4,5)P_2 was modulated by both Ca^{2+} and voltage (Fig. 1B-D). At all voltages, ΔI_{PIP2} was greatest at lower Ca^{2+} concentrations (Fig. 1D). With 270 nM Ca^{2+}, ΔI_{PIP2} at +100 mV was 79.1%, while with 1.1 μM Ca^{2+} ΔI_{PIP2} was <10%. Moreover, at all Ca^{2+} concentrations except the lowest [Ca^{2+}] tested (270 nM), current stimulation by PI(4,5)P_2 decreased with depolarization (Fig. 1C). For example, with 360 nM Ca^{2+} at -100 mV ΔI_{PIP2} was 83.8 ± 30%, but at +100 mV ΔI_{PIP2} was only 37.5 ± 9.1%. The IC_{50} for Ca^{2+} suppression of the PI(4,5)P_2 effect was determined by fitting the data in Fig. 1D to exponential equations. The estimated IC_{50} for attenuation of the diC8-PI(4,5)P_2 stimulatory effect was 390 nM Ca^{2+} at 100 mV and 656 nM Ca^{2+} at -100 mV (Fig. 1D). Because ANO1 has a lower affinity for Ca^{2+} at hyperpolarized potentials (46), the observation that PI(4,5)P_2 has a larger effect at hyperpolarized potentials and at lower Ca^{2+} concentrations indicates that the lipid stabilizes the open, Ca^{2+}-liganded state of the channel. At saturating Ca^{2+} concentration, PI(4,5)P_2 has no additional effect.

The Effect of PI(4,5)P_2 is Specific and Moderate Affinity.

We compared the effects of two other physiologically important phosphoinositides (dioctanoyl phosphatidylinositol 3,4,5-trisphosphate [diC8-PI(3,4,5)P_3] and dioctanoyl phosphatidylinositol 3,5-bisphosphate [diC8-PI(3,5)P_2]) (47, 48) on ANO1 currents (Fig. 2). diC8-PI(3,4,5)P_3, which has one additional phosphate at the 3-position, was less than half as efficacious at

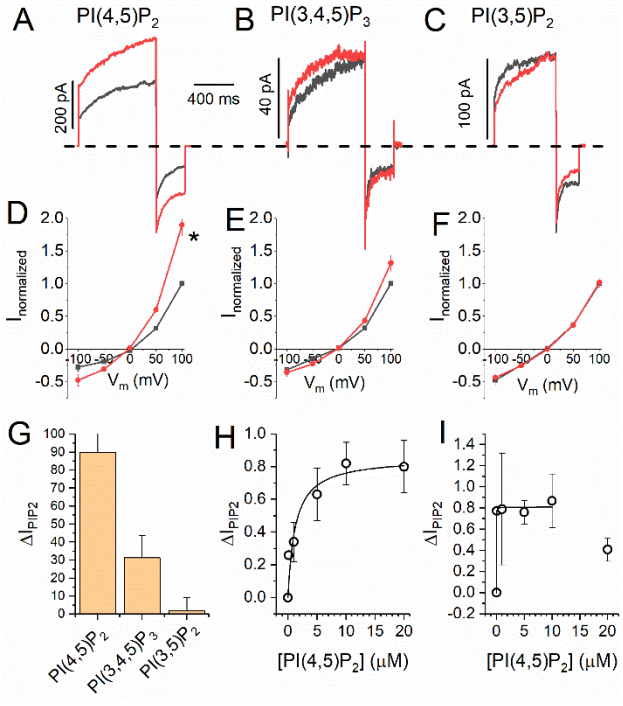

Figure 2. PI(4,5)P_2 effect is selective and moderately high affinity. **(A-C)** Representative current traces at +100 mV with 270 nM Ca^{2+} in the absence (black) and presence (red) of 10 μM **(A)** diC8-PI(4,5)P_2, **(B)** diC8-PI(3,4,5,6)P_3, **(C)** PI(3,5)P_2. **(D-F)** Average ANO1 current voltage relationships in the absence of phosphoinositides (black squares) and in the presence of 10 μM **(A)** diC8-PI(4,5)P_2, **(B)** diC8-PI(3,4,5,6)P_3, **(C)** PI(3,5)P_2. **(G)** Summary of stimulatory effect of phosphoinositides on ANO1 current at 100 mV with 270 nM Ca^{2+}. **(H-I)** Concentration-response curve for diC8-PI(4,5)P_2 on ANO1 current with 270 nM Ca^{2+}at **(H)** 100 mV and **(I)** -100 mV.

10 μM as diC8-PI(4,5)P_2: ANO1 current increased 31 ± 12 % (Fig. 2B,E,G). diC8-PI(3,5)P_2, which has a phosphate in the 3-position instead of the 4-position had no effect at 10 μM (Fig. 2C,F,G). Thus, the effect of PI(4,5)P_2 on ANO1 exhibits specificity.

To estimate the apparent EC_{50} for PI(4,5)P_2, we measured ΔI_{PIP2} in response to different diC8-PI(4,5)P_2 concentrations. The data, fitted to the Michaelis-Menton equation, gave an EC_{50} = 1.24 μM (Fig. 2H) at 100 mV with 270 nM Ca^{2+}. This falls within the range for the effect of PI(4,5)P_2 on other ion channels (0.12 - 4.6 μM, (49-51)). At -100 mV, inward currents were more sensitive to diC8-PI(4,5)P_2 with EC_{50} < 0.1 μM (Fig. 2I).

Selection of Potential PI(4,5)P_2 Regulatory Sites.

To identify amino acids that might play a role in PI(4,5)P_2 regulation of ANO1, we mutagenized amino acids singly or in groups and tested whether stimulation of ANO1 currents in excised patches by diC8-PI(4,5)P_2 was altered. We focused on basic amino acids because known PI(4,5)P_2 binding sites contain two or more positively charged amino acids (38, 52). There are 62 Lys and 60 Arg residues in mouse ANO1. To narrow candidate residues for mutagenesis, we identified Lys and Arg residues located within 10 Å of the cytoplasmic membrane

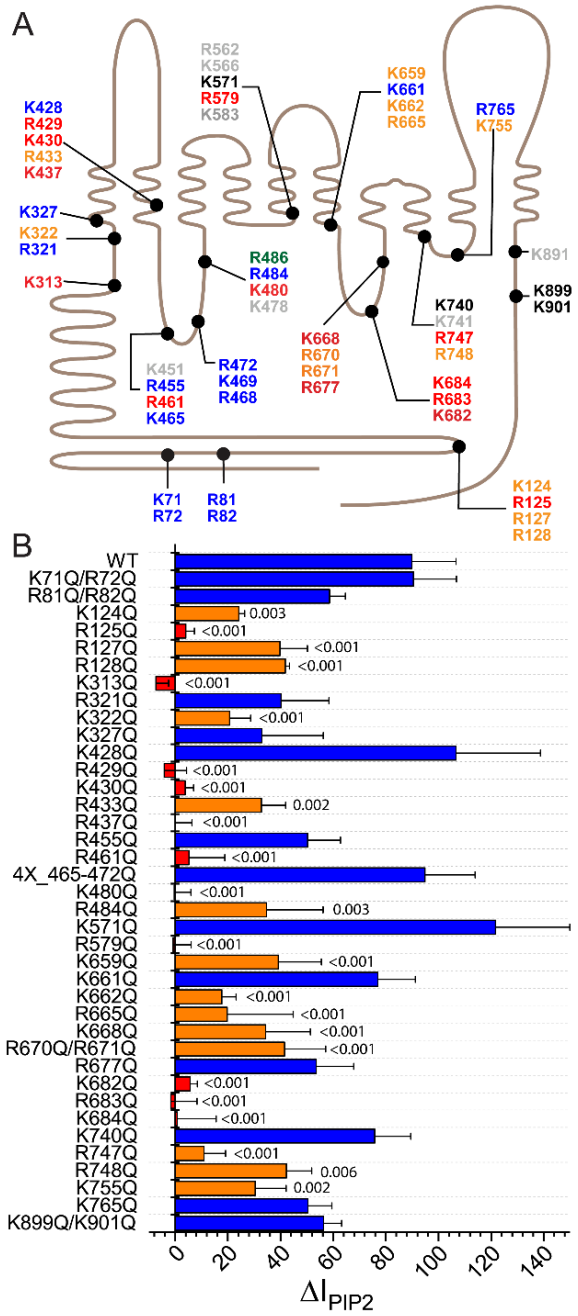

Figure 3. Amino acids involved in mediating the effect PI(4,5)P_2 on ANO1. **(A)** Schematic of 51 basic amino acids that were considered potential PI(4,5)P_2 interacting residues. ANO1 is represented as a line with 10 transmembrane helices. Extracellular is upwards. The length of the line is scaled to the amino acid sequence. Colors indicate effect of mutagenesis on stimulation of ANO1 current by PI(4,5)P_2 corresponding to panel B: Black, response was like WT; Red, PI(4,5)P_2 effect was essentially abolished; Orange: PI(4,5)P_2 effect was significantly reduced; Grey: not tested. **(B)** Effects of mutation of basic amino acids in ANO1 on the stimulation of ANO1 current in inside-out patches by PI(4,5)P_2. 10 μM PI(4,5)P_2 stimulates ANO1 current by ΔI_{PIP2} = 89.9%. Error bars are ± S.E.M. n = 3 -13 patches per mutation. Numbers above bars show statistical P calculated by one-way ANOVA with Fisher LSD post-hoc analysis for difference between means. Blue bars: P >0.05. Orange bars: P <0.05 and >50% reduction in response to PI(4,5)P_2. Red bars: P <0.01 and >90% reduction in response to PI(4,5)P_2.

interface. To this list, we added amino acids in the cytoplasmic N-terminus: K71, R72, R81, and R82 because they are predicted to constitute a phospholipid binding site by BHSEARCH (53), and K124, R125, R127, and R128 because they align partly with a region that ostensibly forms a PI(4,5)P_2 binding site (54, 55) in the ANO1 paralog ANO6 (amino acids 93 – 100) (54, 55) (Fig. 3A).

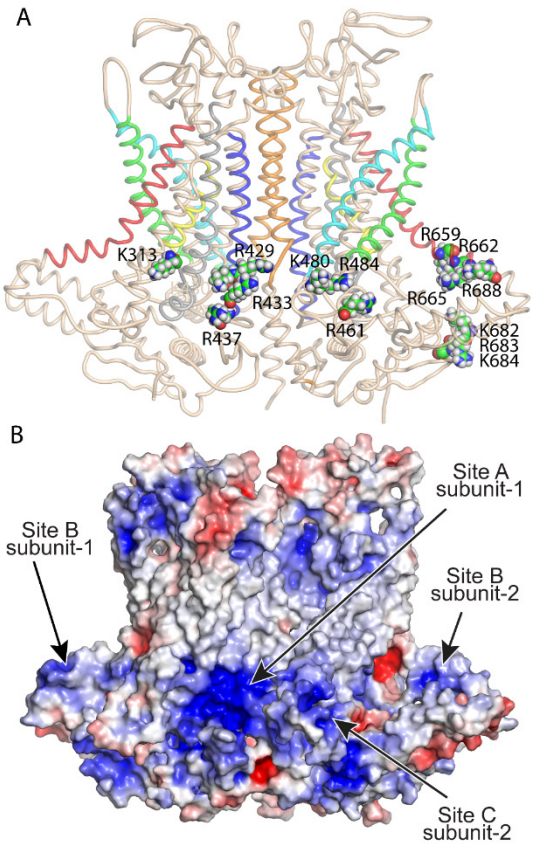

Figure 4. Location of mutations that are critical for the stimulatory effect of PI(4,5)P_2 on ANO1. **(A)** Cartoon representation of ANO1 with critical amino acids as space-fill labeled. For clarity, Site A (K313, R429, K430, R433, R437) is shown only in the left subunit; Site B (K659, R662, R665, R668, R682, R683, and K684) and Site C (R461, K480, and R484) are shown only in the right subunit. Helices are colored, blue (TM2), cyan (TM3), green (TM4), red (TM6), yellow (TM7), and orange (TM10). **(B)** Electrostatic surface of ANO1 calculated by APBS Electrostatics in PYMOL. Red (+5 kT/e), Blue (-5 kT/e).

Mutagenesis to Identify PI(4,5)P_2 Regulatory Sites.

We neutralized the charge on selected Arg and Lys residues by replacement with Gln. Surprisingly, more than 20 mutants were found to have a statistically significant reduction in response to diC8-PI(4,5)P_2 compared to WT. For WT ANO1, $\Delta I_{PIP2} = 89.9 \pm 16.8\%$ (n = 13) in this set of experiments. ΔI_{PIP2} for "significant" mutants was <40% ($p < 0.05$, Fig. 3B orange and red bars). Eleven amino acids were considered "critical" for PI(4,5)P_2 regulation of ANO1 because their mutation reduced ΔI_{PIP2} to <10% (Fig. 3B, red bars).

These critical residues define three locations in the ANO1 structure that correspond to pockets of surface electronegativity (Fig. 4). In the following description, the number in parenthesis is ΔI_{PIP2} when this amino acid is substituted with Gln (WT = 89.9%). Site A is near the dimer interface and is defined by critical amino acids R429 (-4%), K430 (4%), and R437 (0%) in TM2 and K313 (-8%) preceding TM1. R433 (33%), located one helix turn from K430, also contributes to this site. Site B is located at the cytoplasmic end of TM6, which plays a central role in ANO1 gating. It is defined by K682 (6%), R683 (-2%), and K684 (1%). Three nearby amino acids also significantly reduce the effect of PI(4,5)P_2: K662 (18%), K668 (38%), and K665 (22%). Site C is located in the short intracellular loop between TM2 and TM3 that forms one side of the Cl^- ion permeation pathway. It is defined by R461 (6%), K480 (0%), and R484 (39%).

Microscopic Characterization of PI(4,5)P_2 – ANO1 Interaction.

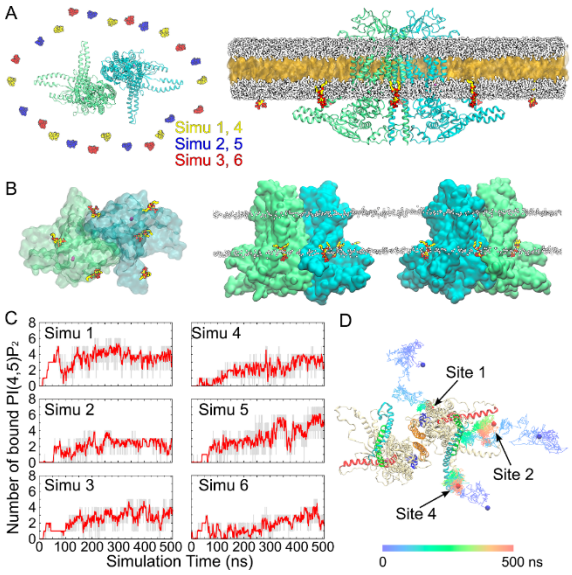

Figure 5. Spontaneous PI(4,5)P_2 binding captured in MD simulations. **(A)** (left) Top view showing the initial placement of eight PI(4,5)P_2 molecules in the inner leaflet of the bilayer surrounding the channel. Six independent simulations were performed with PI(4,5)P_2 molecules placed in different initial positions, as shown by different colors. The two subunits of ANO1 are shown in green and blue, respectively. (right) The initial HMMM simulation system viewed from the membrane, in which a large fraction of the acyl tails of the membrane-forming lipids is replaced by a liquid organic phase (yellow surface representation). The short-tailed POPC molecules are shown in white. The short-tailed PI(4,5)P_2 molecules are shown in color (oxygen: red, phosphorus: tan, carbon: yellow). Ions and water molecules are not shown for clarity. **(B)** Top and side views showing the positions of the PI(4,5)P_2 molecules at the end of one representative HMMM simulation (simu 5). Six PI(4,5)P_2 molecules were found to be directly coordinated by the charged/polar residues of the channel. Ca^{2+} ions are shown as purple spheres. The membrane position is demarcated by the phosphorus atoms (white spheres) of the PC lipids. **(C)** Number of bound PI(4,5)P_2 molecules (grey trace) and the moving average (red, bin=20) plotted vs. simulation time for the six simulations. **(D)** Representative trajectories showing the binding of PI(4,5)P_2 to Sites 1, 2, and 4. The colored lines illustrate the position of the 4'-phosphate of PI(4,5)P_2 over the 500-ns simulations at 100-ps intervals. The initial and final positions of the 4'-phosphate are shown as blue and red spheres, respectively.

In order to gain more insight into the binding of PI(4,5)P_2 t o ANO1, we performed molecular dynamics (MD) simulations using the highly mobile membrane mimetic model (HMMM) (54,59). The HMMM model was introduced to accelerate lipid diffusion in atomistic MD simulations in order to obtain significantly enhanced sampling of interaction of lipid headgroups with proteins within simulation timescales currently achievable. In conventional membrane models, lipids with long acyl chains have a relatively low lateral diffusion constant (~8×10^{-8} cm^2 s^{-1}). Therefore, during a 500 ns simulation, lipids do not diffuse far enough to allow sufficient mixing and sampling of the protein surface. The HMMM model accelerates lipid lateral diffusion by shortening lipid acyl tails to six carbons and filling the membrane core with a liquid phase (Fig. 5A). The HMMM model has been used successfully to study the diffusion and domain formation of lipids and membrane-associated proteins, pore formation by peptides, hydrophobic matching of transmembrane helices, and membrane-associated assembly of coagulation factors (56-64). The purpose of the model is to provide a more flexible and mobile environment that allows for rapid rearrangement and displacement of the lipid headgroups, thereby facilitating phenomena that might be inaccessible with conventional membrane models due to the inherently slow dynamics of the lipids.

To examine the interaction of ANO1 with PI(4,5)P_2, eight C6-PI(4,5)P_2 molecules were added to the inner leaflet of a C6-POPC bilayer evenly surrounding ANO1 (Fig. 5A) at the beginning of the simulation. C6-PI(4,5)P_2 constitutes ~1.4 mol% of the total lipids in the inner leaflet. To diminish any bias introduced by the initial placement, the position of the PI(4,5)P_2 molecules were shifted in each of the six independent simulations such that

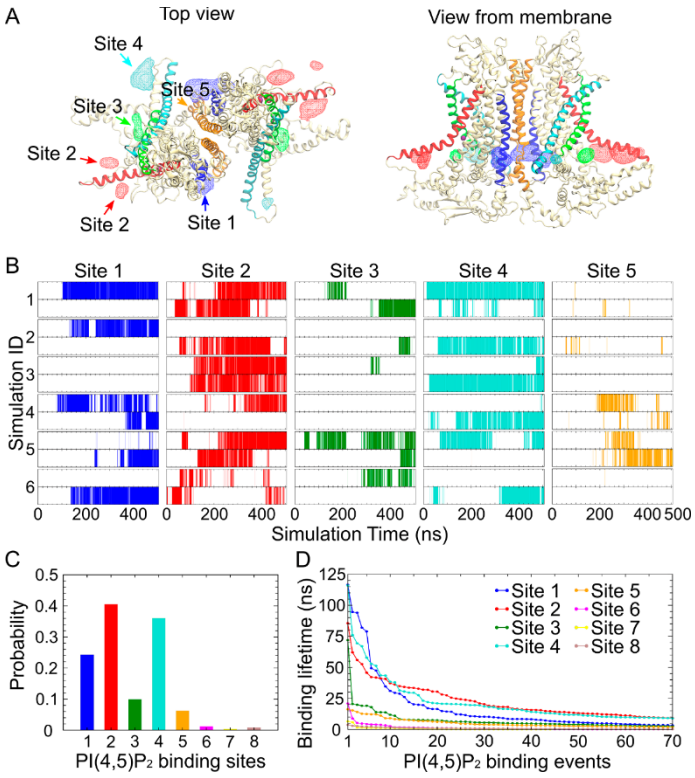

Figure 6. PI(4,5)P_2 binding at specific sites on ANO1. **(A)** Volumetric map of inositol occupancy extracted from the last 200 ns of the HMMM simulations is shown as colored wireframe contoured at isovalue 0.05 overlaid on the protein structure. Analysis combines results from the six simulations. Each local map is colored with the same color used for the nearby transmembrane helix that is involved in PI(4,5)P_2 binding (TM2: blue, TM3: cyan, TM4: green, TM6: red, and TM10: orange). **(B)** PI(4,5)P_2 occupancy at Sites 1–5 in each subunit (upper panel: Subunit 1, lower panel: Subunit 2) during the 6 independent PI(4,5)P_2-binding simulations. PI(4,5)P_2 binding is indicated by the vertical lines at the corresponding time point. **(C)** The probability of PI(4,5)P_2 occupancy for each site over the 6 PI(4,5)P_2-binding simulations. PI(4,5)P_2 binding was observed mainly in Sites 1, 2, and 4. **(D)** Dwell time of the top 70 binding events in each of the 8 binding sites, sorted in descending order. Only Sites 1, 2, and 4 exhibit significant dwell times.

each simulation began with different PI(4,5)P_2 starting positions. Within 50 ns, the PI(4,5)P_2 molecules diffused around the protein and interacted with it. The number of bound PI(4,5)P_2 molecules reached a plateau after ~300 ns with an average of 4.5 PI(4,5)P_2 molecules bound per dimer (range 3 – 6) in each simulation at the end of 500 ns (Fig. 5 B,C). Representative trajectories of PI(4,5)P_2 interacting with ANO1 are shown in Fig. 5D. At the end of the six HMMM simulations with C6-PI(4,5)P_2, all subunits had at least one PI(4,5)P_2 molecule bound: two subunits had Site 1 occupied only, six subunits had Site 2 and/or 4 occupied, 4 subunits had Site 1 plus Site 2 and/or 4 occupied.

By calculating the density of the inositol groups over the simulation trajectories and the interactions between the phosphate/hydroxyl groups of PI(4,5)P_2 and ANO1, eight sites on the cytoplasmic surface of ANO1 were found to be visited by PI(4,5)P_2 molecules. Sites 1–5 (labelled according to their clockwise location) involve basic and aromatic residues at the membrane-cytoplasm interface around the ends of transmembrane helices TM1, TM2, TM3, TM4, TM6, and TM10 (Fig. 6A). PI(4,5)P_2 binding to these sites was observed in multiple independent trajectories and for both subunits of ANO1 (Fig. 6B), revealing several specific and stable interactions between PI(4,5)P_2 and the protein. Sites 6–8, which bind PI(4,5)P_2 only transiently, mainly involve residues from the N-terminal region of ANO1, including the short α-helices α0a and α0b and the loop preceding them, and the loop between Nβ1 and Nα1. Among the eight sites captured in the simulations, Sites 1, 2, and 4 showed the highest occupancies (Fig. 6C). These three sites represent 84.3% of all the binding events observed. PI(4,5)P_2 headgroups are well coordinated in these binding sites, resulting in residence

lifetimes as long as 116.5 ns (Fig. 6D). Because PI(4,5)P_2 binding to Sites 1, 2, and 4 was more robust than binding to the other sites, we focused on these three sites for further analysis.

Insight Into the Functional Roles of Specific Key Amino Acids. In Site 1, five basic residues (R433, K430, R429, R437, and K313, Fig. 7A,D), which stabilize the binding of PI(4,5)P_2 by coordinating the inositol ring and its phosphates. All of these residues are experimentally verified to strongly affect PI(4,5)P_2 binding (Fig. 3B). Of the four residues that coordinate PI(4,5)P_2 for >10% of the total residence time in Site 1, K430 shows strong preference for interaction with the hydroxyl groups on the inositol ring, while the other three basic residues mainly coordinate 4'- and 5'-phosphate groups. R437 is located closer to the cytoplasm than the other residues and interacts almost exclusively with the 4'- and 5'-phosphate groups. This feature suggests that R437 might be crucial for specific recognition of PI(4,5)P_2. Experimentally, the R437Q mutation totally abolishes the PI(4,5)P_2-induced effect. Similarly, in Site 2 (Fig. 7B,E), all the residues facing the cytoplasm including those in the cytoplasmic loop connecting TM6 and TM7 (R677, R683, K682, K684) and R665 in TM6 are mainly involved in coordinating the 4'- and 5'-phosphate groups. The other residues in TM6 show less discrimination and also interact with the 1'-phosphate and hydroxyl groups on the inositol ring. In Site 4 (Fig. 7C,F), all major interacting residues show preference for 4'- and 5'-phosphate groups except for R484, which indiscriminately coordinates all the functional groups on the inositol ring.

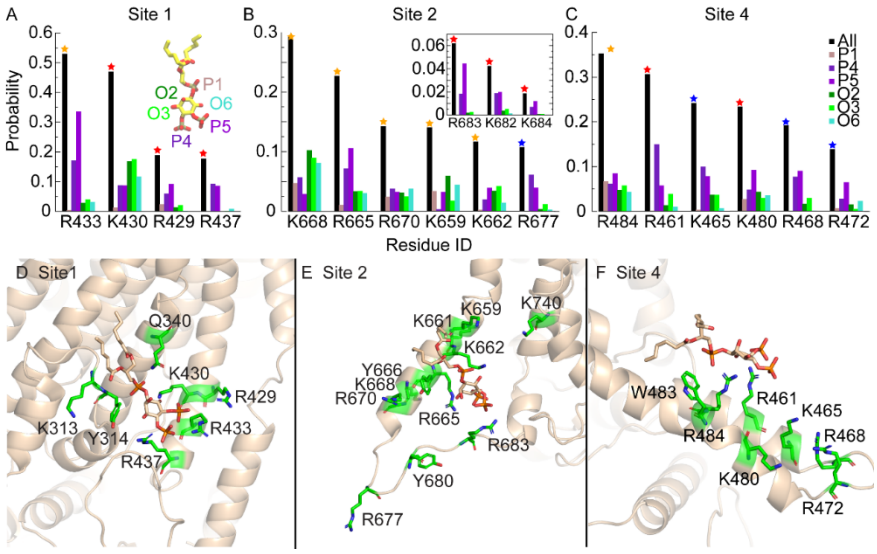

Figure 7. PI(4,5)P_2 coordination in major binding sites. **(A-C)** The probability of PI(4,5)P_2 headgroup coordination by the key basic residues in Sites 1, 2, and 4 is shown as black bars. Residues that coordinate PI(4,5)P_2 for >10% of the total binding time in each site are shown (other residues that affect PI(4,5)P_2 binding experimentally are also shown in the inset). The color of the star on each bar represents the experimental results in Figure 3(B), where the mutation of the residues affects PI(4,5)P_2 binding to different degrees. The coordination probability for each functional group on the inositol ring (1'-phosphate, 4'-phosphate, 5'-phosphate, 2'-hydroxyl, 3'-hydroxyl, and 6'-hydroxyl) is shown individually. **(D-F)** Coordination of PI(4,5)P_2 in Sites 1, 2, and 4. Amino acids that interact with each binding site are shown as stick representation in green. PI(4,5)P_2 is shown in stick representation in tan.

Specificity of Phospholipid Binding. To evaluate the specificity of PI(4,5)P_2 binding, we measured the effect of PtdSer on PI(4,5)P_2 binding by performing three 350-ns simulations with a mixture 8 PI(4,5)P_2 and 8 PtdSer molecules with each simulation having a different initial

placement of the lipids. On average, the number of bound $PI(4,5)P_2$ molecules over the trajectories was reduced ~20% from 2.73 ± 1.28 to 2.21 ± 1.45 (per monomer), which was not statistically significant. In these simulations, $PI(4,5)P_2$ interacted with 42 residues. We analyzed whether the $PI(4,5)P_2$ coordination probability was different for these 42 residues in simulations with and without PtdSer and found that they were not statistically different (one way ANOVA, $p>0.1$). In contrast, PtdSer binding to these sites was significantly different than $PI(4,5)P_2$ in the same simulations ($p<0.001$). In these simulations, the PtdSer headgroup only interacted with seven residues with significant probability (>0.01). Two residues are in Site 1 (R429: 0.09; R433: 0.06), one in Site 2 (R670: 0.02), two in Site 4 (R461: 0.02, K465: 0.01), and two others near Site 4 (R486: 0.04, K469: 0.01). These data suggest that although PtdSer may also bind to these sites, $PI(4,5)P_2$ has a higher probability of interaction.

Potential Conformational Changes Induced by $PI(4,5)P_2$. To determine whether binding of $PI(4,5)P_2$ was influenced by full-length acyl chains, the short-tailed lipid molecules (C6-$PI(4,5)P_2$ and C6-POPC) used in the initial probing of lipid-protein interactions were converted back to full-length lipids (palmitoyl-oleoyl-$PI(4,5)P_2$ and palmitoyl-oleoyl-POPC) at the end of the HMMM simulations, and the resulting full systems were subjected to an additional equilibrium simulation of 600 ns. During these simulations with full-length lipid, each bound $PI(4,5)P_2$ molecule remained coordinated around its binding site, suggesting that these sites stably bind full-length $PI(4,5)P_2$. In the HMMM simulations, the $PI(4,5)P_2$ molecules were more likely to dissociate from their binding sites and sample more binding events.

We compared the conformation of the $PI(4,5)P_2$-bound ANO1 with its conformation in a control simulation performed in the absence of $PI(4,5)P_2$. The most significant change captured in the simulations with $PI(4,5)P_2$ bound is a rotation of the cytoplasmic half of TM6, which forms one side of the channel pore and plays a key role in channel gating (Fig. 8A,B). The position of the cytoplasmic portion of TM6 is described by two angles. α is the angle of TM6 projected onto the x-y plane with the position in the cryo-EM structure defined as 0°. β is the angle of TM6 relative to the x-y plane. In the absence of $PI(4,5)P_2$, the cytoplasmic end of TM6 fluctuates only slightly around its initial position (peak $\alpha = 0^o$, peak $\beta = 36^o$). When any site is occupied at Sites 2/4, or single occupancy at Site 1, there is a significant shift of TM6 away from the pore (peak $\alpha = 12^o – 18^o$, peak $\beta = 22^o$). When Site 1 plus Site 2 and/or 4 are occupied, there is an even more dramatic rotation of the cytoplasmic end of TM6 away from the pore (peak $\alpha = 18^o – 32^o$, peak $\beta = 22^o$).

When $PI(4,5)P_2$ was bound, penetration of Cl^- ions into the pore was frequently observed (Fig. 8C). Especially in the case of the multi-occupied simulations (sites 1 and 2/4), deep penetration of Cl^- occurred ~25% of the total time. The major Cl^--coordinating amino acids were K588, K645, N650, and Q646. S592 also participated when Cl^- entered more deeply. Although we had hoped to observe Cl^- ions transiting the entire conduction pathway, this did not happen in the timeframe of our

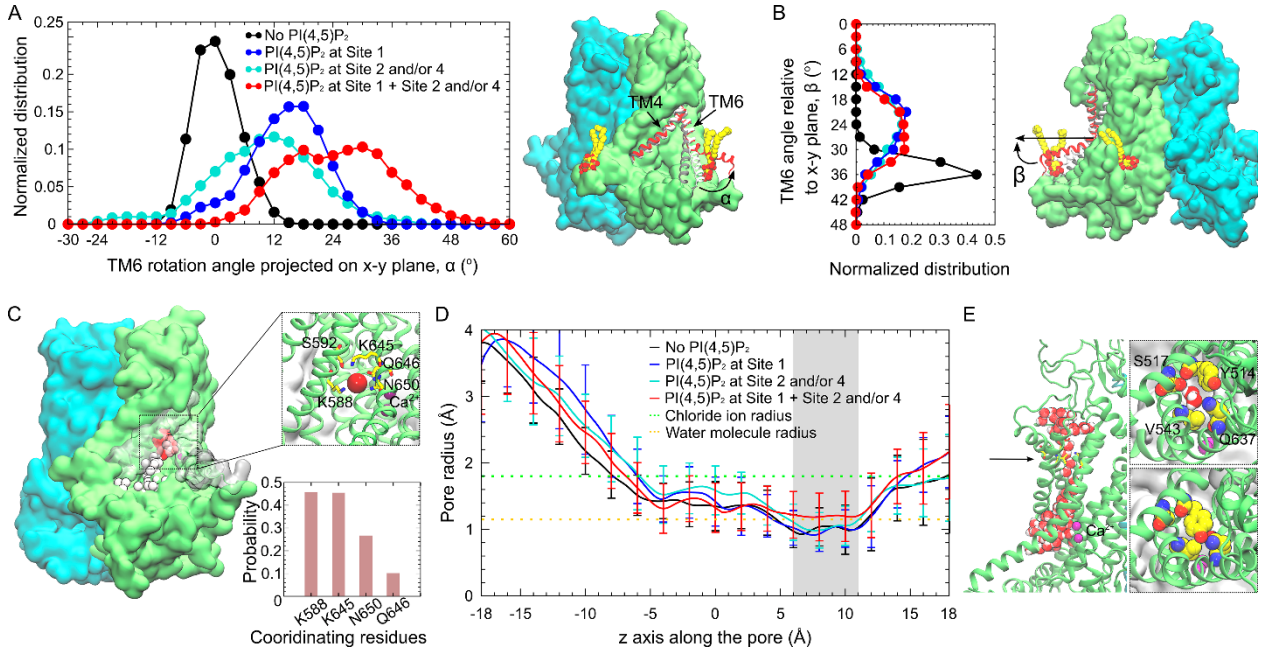

Figure 8. Conformational changes induced by PI(4,5)P_2 binding. **(A)** Rotation angle of the cytoplasmic portion of TM6 with respect to its position in the cryo-EM structure, projected onto the x-y plane. Left panel: Distribution of the rotation angle normalized over the 600 ns full-length lipid simulations for each palmitoyl-oleoyl PI(4,5)P_2 occupancy state. The cytoplasmic portion of TM6 fluctuates around its initial position (0°) in the absence of PI(4,5)P_2 (black). Single occupancy of Site 1 (blue), or single/double occupancy of Sites 2 and 4 (cyan) shifts the rotation angle to positive values (cytoplasmic portion of TM6 away from the pore). Multiple occupancy of PI(4,5)P_2 at Sites 1 plus 2 and/or 4 (red) rotates TM6 most dramatically away from the pore. Right panel: Snapshots of TM6 in the multiply-occupied state (red), the PI(4,5)P_2-free state (black), and the cryo-EM structure (white). Bound PI(4,5)P_2 is shown in vdW representation. **(B)** Left panel: Distribution of the angle between the TM6 cytoplasmic portion and the x-y plane. Right panel: Snapshot showing the angle relative to the membrane in the multiple-occupied state (red), the PI(4,5)P_2-free state (black), and the cryo-EM structure (white). **(C)** Time series snapshots showing the spontaneous penetration of Cl^- ions (vdW spheres, white-to-red over time) in the multiply-occupied state. Coordination of the Cl^- ion deeply binding inside the pore is shown in the inset, with the probability of coordination for all the binding events shown below. Cl^- and Ca^{2+} ions are shown as red and purple spheres, respectively. **(D)** Average radius of the ion conduction pore calculated using HOLE (86) illustrates a bottleneck between 6 and 11 Å (grey shading). The bottleneck in the multiply-occupied state dilates ~30% compared to other states. Orange dotted line: radius of water molecule (1.15 Å). Green dotted line: radius of Cl^- ion (1.8 Å). **(E)** Left panel: Hydration of the ion conduction pore when the bottleneck (black arrow) dilates in the multiply-occupied state. Right panel: Top views of the pore showing the amino acids forming the bottleneck. The sidechain orientation of Y514 affects the pore radius and hydration.

simulations. However, these simulations were performed with no applied voltage. Without driving force for Cl^- movement, ion conduction may be too slow to capture in this 600 ns simulation. Further, the voltage-dependent gating of ANO1 was not activated, so the conditions for the protein entering a conducting state may be sub-optimal. The cryo-EM model of ANO1 we used for these simulations is a non-conducting state with a constriction in the pore between 6 and 11 Å formed by the bulky residue Y514 and three nearby residues (S517, V543, and Q637). When multiple PI(4,5)P_2 sites are occupied (site 1 and 2/4), we observed that the conduction pathway dilated ~30% to a radius of 1.2 Å (Fig. 8D,E), which is slightly greater than the radius of a water molecule (1.15 Å), but is smaller than

a Cl^- ion (1.8 Å). Thus, forces that stabilize this non-conducting conformation are apparently sufficiently strong to prevent pore opening in the timeframe of these simulations.

Discussion

Correspondence between Mutagenesis and MD Predictions. In this study, we used mutagenesis and computational modeling to identify lipid-binding sites in ANO1 that are important in regulation of the channel by $PI(4,5)P_2$. Sites 1, 2, and 4 predicted by MD simulations to capture 84% of all interactions between ANO1 and $PI(4,5)P_2$ correspond topographically to Sites A, B, and C determined by mutagenesis. In further commentary, these sites are referred to as Sites A/1, B/2, and C/4.

Both the mutagenesis and computational approaches have their limitations. Mutagenesis experiments can identify sites that are important in functionally mediating the effect of $PI(4,5)P_2$ on ANO1, but this approach cannot easily distinguish between amino acids that coordinate $PI(4,5)P_2$ binding, stabilize the structure of the binding site, or allosterically couple $PI(4,5)P_2$ binding to channel gating or ion permeation. Furthermore, it should be noted that amino acids critical for the $PI(4,5)P_2$ effect were identified under very specific recording conditions of 270 nM Ca^{2+} and 100 mV. Given the sensitivity of the $PI(4,5)P_2$ effect to both voltage and Ca^{2+}, it is entirely possible that under different conditions where ANO1 occupies different conformational states, a different complement of amino acids may be involved in mediating $PI(4,5)P_2$ binding and effect. The MD simulations provide direct information about amino acids that are energetically favorable for binding $PI(4,5)P_2$, but suffer from incomplete knowledge about native ANO1 and membrane structure in living cells. Furthermore, the MD simulations were not performed under identical conditions as the live-cell patch clamp experiments. For example, no voltage was applied during the MD simulations and there was no free Ca^{2+} present in the system. While the correspondence between the functional live-cell experiments and the MD simulations is not perfect, the global agreement is remarkable. This provides a high level of confidence that these sites are involved in $PI(4,5)P_2$ binding.

Site A/1 is the most robust site we have identified with all the same amino acids identified in mutagenesis and MD (Table I). Mutation of a single amino acid (R429, K430, R437, or K313) in this site nearly abolishes the effect of $PI(4,5)P_2$. The MD simulation shows the headgroup of $PI(4,5)P_2$ is well-coordinated by a pocket formed by R429, K430, and R437 on one side and K313, Y314, and Q340 on the other sides (Fig. 7D). The site fulfils the requirements for a canonical $PI(4,5)P_2$ binding site by having at least one Lys (K430) and one aromatic amino acid (Y314).

A close agreement also exists between the MD and functional studies for Site B/2 (Table I). By both MD and mutagenesis, Site B/2 is composed of at least six basic amino acids, only one of which (R683) is essential for the $PI(4,5)P_2$ effect. Mutation of each of the other amino acids has a partial effect, but this agrees with the modest probability of each of these amino acids coordinating

$PI(4,5)P_2$. Site B/2 also resembles a bona-fide $PI(4,5)P_2$ binding pocket (aromatic Y666 and Lys K684) (Fig. 7E).

Site C/4 has both Lys and aromatic residues but does not form a pocket and may be an electrostatic CALM-type $PI(4,5)P_2$ binding site (Fig. 7F). Mutation of K480 abolishes the response to $PI(4,5)P_2$, and mutation of R461 and R484 have a significant effect. However, mutation of the other three basic residues identified by MD has no effect.

In addition to these 3 major sites, mutagenesis identified several amino acids outside these sites. We suspect that some of these amino acids may play structural or allosteric roles. R579 makes a hydrogen bond with E568 in the loop between TM4 and TM5, which are important in forming the conduction pathway. R747 forms hydrogen bonds with L693 and E694 (L693:O-K747:NE and E694:O-K747:N), which lock the cytoplasmic ends of TM7 and TM8. This may be important in maintaining a proper conformation of Site B/2 (K682, R683, and R684) to interact with $PI(4,5)P_2$. Mutation of R125 and its adjacent amino acids in the N-terminus significantly affect $PI(4,5)P_2$ binding, but interpretation is hampered because the N-terminus is not modeled well in the cryo-EM structures (see below).

Role of the N-terminus. It has been reported that ANO6, a paralog of ANO1 with 54% sequence similarity, is regulated by $PI(4,5)P_2$ binding to the N-terminus (54, 55). Ye et al. (55) showed that mutation of amino acids K87, K88, K95, R96, K97, and R98 decreases the Ca^{2+}-sensitivity and reduces the ability of exogenously-applied $PI(4,5)P_2$ to restore ANO6 current after rundown. ANO6 residues 95-KRKR-98 align in PROMAL3D with ANO1 residues 124-KRFRR-128, and alignment of the ANO1 (5oyb) and ANO6 (6qp6) structures shows these sequences are similarly located in the protein structure. Although we find that mutation of these residues in ANO1 decreases the responsiveness to $PI(4,5)P_2$, the N-terminus is not well resolved in the ANO1 structure, and amino acids 1-116 and 131-164 are not modeled. Thus, it remains unclear how these amino acids contribute to ANO1 regulation. Also, the role of these amino acids in ANO6 remains in question because Aoun et al. (54) showed that deletion or mutagenesis of this site in ANO6 had no effect on $PI(4,5)P_2$ binding. Rather, they propose that amino acids 302-KKQPLDLIRK-311 in the proximal N-terminus of ANO6 are important for $PI(4,5)P_2$ binding. This sequence aligns well with 313-KKQPLDLIRK-322 in ANO1, and we find that mutation of K313 in ANO1 significantly reduces the stimulatory effect of $PI(4,5)P_2$ on ANO1 current. K313 is located in a re-entrant membrane loop just before TM1 in both ANO1 and ANO6 structures and is a crucial residue in Site A/1.

A Network of $PI(4,5)P_2$ Binding Sites. A major question raised by this study is "Why does ANO1 have multiple $PI(4,5)P_2$ binding sites and what are their functions?" Most studies on $PI(4,5)P_2$-protein interaction generally assume that the effect of $PI(4,5)P_2$ is mediated by a single binding site. However, there are several examples of proteins interacting with $PI(4,5)P_2$ in different ways. For

example, X-ray crystallography, coarse-grained MD, and reconstitution in artificial membranes have demonstrated that the Arf GTPase and its GEF Brag2 form a complex that binds to the membrane via multiple PI(4,5)P_2 interaction sites (65). There is also some mutational and biochemical evidence for multiple PI(4,5)P_2 binding sites on profilin-1, gelsolin, TRPV1, EAG1, and K_{ir}2.1 (66-70).

We anticipate that the three PI(4,5)P_2 binding sites in ANO1 may have different and/or interacting effects. Although considerable work will be required to dissect these functional consequences, at this point in time we propose a general model for ANO1 gating that involves the binding of Ca^{2+} and PI(4,5)P_2 to regulate this complex channel (Fig. 9). One corollary conclusion of

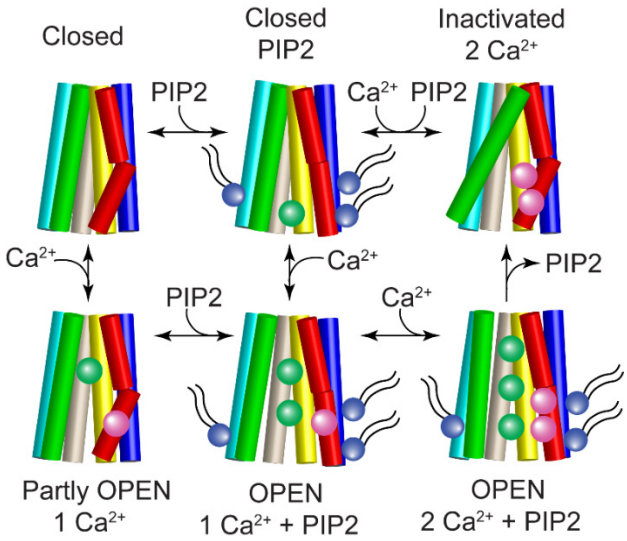

Figure 9. Cartoon model of ANO1 gating. TM2 (blue), TM3 (cyan), TM4 (green), TM5 (wheat), TM6 (red), and TM7 (yellow) are shown as cylinders. The pore is formed by TM4-TM7 and Ca^{2+} (magenta spheres) binds to residues in TM6 and TM7. When PI(4,5)P_2 (purple sphere with tails) binds to the cytoplasmic ends of TM2 (Site A/1), TM6 (Site B/2), and TM3 (Site C/4), the cytoplasmic end of TM6 swings away from the pore to ultimately open the cytoplasmic vestibule to Cl^- (green spheres). Top row: the channel is closed in the absence of Ca^{2+} and inactivated when two Ca^{2+} ions are bound in the absence of PI(4,5)P_2. Bottom row: the channel can partly open when one Ca^{2+} binds in the absence of PI(4,5)P_2 but full channel opening requires both Ca^{2+} and PI(4,5)P_2.

this model is that the cryo-EM structures of ANO1 that have been published (22, 23) represent the inactivated state because the channel does not have PI(4,5)P_2 bound.

The locations of the three sites in the protein may provide some insights into their possible function. Key residues forming Site A/1 are located in TM1, TM2, and the loop between α0a and α0b. Because TM1 and TM2 are tightly packed against TM7 and TM8 that harbor part of the Ca^{2+} binding site, PI(4,5)P_2 binding to Site A/1 could have widespread allosteric effects on Ca^{2+} sensitivity and could be responsible for stabilizing the Ca^{2+}-bound open state. Site B/2 is formed by amino acids at the cytoplasmic end of TM6 and intracellular loop 3 **(ICL3)** connecting TM6 and TM7. TM6 plays a crucial role in ANO1 gating (24, 25, 30) so that its conformational changes could alter channel gating. Also, TM6 and TM7 harbor three amino acids that form the binding site for Ca^{2+}, so PI(4,5)P_2 binding to this site could also affect Ca^{2+}-dependent gating. Site C/4 is located at the cytoplasmic end of TM3 in the loop connecting TM3 and TM2. TM3 is tightly packed with TM4 that lines the conduction pathway, so binding of PI(4,5)P_2 to Site C/4 could modify the ion conduction pathway.

Methods

Cell Culture and Transfection. HEK-293 cells (ATCC) were maintained in modified DMEM with 10% FBS, 100 U/ml penicillin G and 100 μg/ml streptomycin) and transiently transfected with mTMEM16A (Uniprot Q8BHY3). HEK293 cells were authenticated by short tandem repeat profiling and were tested for myoplasm contamination. TMEM16A was tagged on the C-terminus with EGFP. PCR-based mutagenesis was used to generate single amino acid mutations. Mutations were verified by sequencing.

Phosphatidylinositols and Inositol Phosphates. Phosphatidylinositols were purchased from Echelon Research Laboratories (Salt Lake City, UT). Unless noted otherwise, the synthetic lipids used in these experiments have C8 saturated fatty acid chains. At concentrations used here, these short chain phosphoinositides are likely monodisperse in solution. It has been estimated that the critical micelle concentration (CMC) for lipids with phosphorylated inositol headgroups is >3 mM (71). Stock solutions of 10 mM PI(4,5)P_2 were made in deionized H_2O and stored at -20°C. Working solutions were made fresh immediately before the experiment.

Preparation of the ANO1 Structure for Simulation. The cryo-EM structure of mouse TMEM16A (PDB 5OYB) at 3.75 Å resolution (72) was used as the starting structure for the MD simulations. Nomenclature of alpha-helices is from ref. (72). Because amino acids 1-116 (N-terminus), 131-164 (N-terminus), 260-266 (N-terminus), 467-487 (TM2-TM3 linker), 669-682 (TM6-TM7 linker), and 911-end (C-terminus) are unstructured in the cryo-EM model, we used a model in which the TM2-TM3 and TM6-TM7 linkers and N-terminal residues 131-164 and 260-266 were added using SuperLooper2 (73) and subjected to energy minimization. The two Ca^{2+} ions bound in each of the two subunits were preserved for all the simulations. The pKa of each ionizable residue was estimated using PROPKA (74, 75) and default protonation states were assigned based on the pKa analysis. Missing hydrogen atoms were added using PSFGEN in VMD (76). Internal water molecules were placed in energetically favorable positions within the protein using DOWSER (77, 78).

Simulation System Setup. The ANO1 protein was first embedded in a palmitoyl-oleolyl phosphatidylcholine (POPC) bilayer generated using the CHARMM-GUI membrane builder (79). In each of the six independent simulation systems (Simu 1 – Simu 6), eight PI(4,5)P_2 molecules were evenly placed around the protein in the inner leaflet of the membrane (~1.4% PI(4,5)P_2) (Fig. 5A). PI(4,5)P_2 molecules were parameterized using CHARMM36 parameters. Considering the possible protonation states of PI(4,5)P_2, two variations of PI(4,5)P_2 headgroups were used in the simulations: systems 1–3 used palmitoyl-oleoyl-phosphatidylinositol-(4,5)-bisphosphate with protonation on P4, while systems 4–6 used the palmitoyl-oleoyl-phosphatidylinositol-(4,5)-bisphosphate with protonation on P5. The initial positions of the PI(4,5)P_2 molecules were at least 30 Å away from any atom of the channel. The membrane was then converted to a highly mobile membrane memetic (HMMM) model using in-house scripts. This model replaces a portion of the membrane hydrophobic core by a more fluid representation using simple carbon solvent ethane (SCSE), while using short-tailed lipids to

maintain full description of the headgroups and the initial part of the tails. The membrane/protein systems were fully solvated with TIP3P water (80) and buffered in 150 mM NaCl to keep the system neutral. The resulting systems consisting of ~575,000 atoms were contained in a 244×180×141 $Å^3$ simulation box.

To evaluate the specificity of $PI(4,5)P_2$ binding to the channel, an additional set of simulations (3 trajectories, 350-ns each) were performed with 8 PtdSer molecules evenly placed around the protein in the inner leaflet of the membrane, in addition to the 8 $PI(4,5)P_2$ molecules. Each simulation of mixed $PI(4,5)P_2$ and PtdSer has a different initial placement of the lipids. The simulation setup was otherwise the same as described above.

Simulation Protocols. MD simulations were carried out with NAMD2.12 (81) using CHARMM36m force field (82) and a timestep of 2 fs. Periodic boundary conditions (PBC) were used throughout the simulations. To evaluate long-range electrostatic interactions without truncation, the particle mesh Ewald (PME) method (83) was used. A smoothing function was employed for short-range non-bonded van der Waals forces starting at a distance of 10 Å with a cutoff of 12 Å. Bonded interactions and short-range non-bonded interactions were calculated every 2 fs. Pairs of atoms whose interactions were evaluated were searched and updated every 20 fs. A cutoff (13.5 Å) slightly longer than the non-bonded cutoff was applied to search for interacting atom pairs. Simulation systems were subjected to Langevin dynamics and the Nosé-Hoover Langevin piston method (84, 85) to maintain constant pressure (P=1 atm) and temperature (T=310 K) (NPT ensemble). To allow the simulation systems to fluctuate in all dimensions, in pressure control, a constant ratio was used for both HMMM and full-length simulations. This parameter keeps the x:y ratio of the unit cell constant rather than keeping the dimensions of the unit cell constant, thus allowing the surface area of the membrane to fluctuate during the simulation.

HMMM Simulations. Because the HMMM representation simplifies the lipid bilayer by making the core more fluid, grid forces were applied on the carbon atoms affected by the conversion from the full-length membrane to the HMMM model to restrain the HMMM lipids, in order to resemble the full-length membrane while still allowing lipid molecules to fluctuate. The target atoms affected by the grid forces included carbon atoms in the solvent SCSE molecules and the terminal carbons (C26 and C36) of the short-tailed POPC and POPI lipids. The aim was to make the positions (z-coordinates) and flexibility of these target atoms resemble their counterparts in full-length membrane. To realize this, 3D grids with 1-Å spacing were specified in the simulation box to define the potential to be applied. Different potential values were then assigned to each grid point depending on the z-position within the membrane (centered at z=0). The grid potential $U_{grid}(z)$ is defined by the equation,

$$U_{grid}(z) = \begin{cases} 0, & z = 0, \pm 1, \dots, \pm 10 \\ k \times (|z| - z_c)^2, & z = \pm 11, \pm 12, \dots, \pm 20 \end{cases}$$

where $k = 0.025 \frac{kcal}{mol \cdot A^2}$, $z_c = 10$ Å, and z denotes the z-position of the grid point. For each target atom within the grid, the force was computed by a tri-cubic interpolation of the potential from the surrounding grid values based on the z-position of the atom. The target atoms thus experience zero or close-to-zero force when they are in the region comparable to that of their counterparts in the full-length membrane (z within ±10 Å); increasing force is experienced when they are diffusing toward the headgroup/bulk-solvent region (z beyond ±10 Å). Since only the terminal carbon atoms (C26 and C36) in the short-tail lipids are affected by the grid forces, this method provides the majority part of the molecules, especially the headgroups, with considerable flexibility in all dimensions during the simulation.

To verify that the HMMM simulations were providing a reasonable model of bilayer, we compared the dynamics of the phospholipids in a simulation of TMEM16A in full-length membrane (600 ns, no restraint) with the HMMM model used here (500 ns). The fluctuations of the choline-nitrogen atoms or phosphate atoms of POPC headgroups in the z-axis were used as metrics. In the HMMM simulations, the z-positions of the choline nitrogens within 10 Å of the protein fluctuate up to 10-10.5 Å in each direction, and phosphorus atoms can fluctuate 9-9.5 Å. The capacity for fluctuation of the headgroup components shows that the model used in this study provides sufficient freedom for the HMMM membrane mimetics to behave similarly to a full-length membrane (56, 64).

The six HMMM simulation systems were first energy-minimized for 10,000 steps followed by a 1-ns relaxation MD, during which the heavy atoms from the protein were positionally restrained (k=1 kcal/mol/Å^2) to allow the *de novo* added structures to relax. Then a 500-ns equilibrium simulation was performed for each system with the Cα atoms of the transmembrane region (estimated using the PPM server) slightly restrained (k=0.1 kcal/mol/Å^2). Our published data showed that using SCSE solvent can greatly improve the behavior of transmembrane proteins within the HMMM model (56). SCSE showed substantially less solvent intercalation into transmembrane proteins compared to DCLE and SCSM solvents in absence of restraint on the proteins (64). Nevertheless, to prevent any potential disruption of the transmembrane structure, we applied a slight restraint on the C-alpha atoms of the transmembrane region of TMEM16A. The rest of the protein (sidechains of the transmembrane region and the backbone atoms and sidechains of the cytoplasmic and extracellular regions) was free to move. Such restraint is not likely to affect the sampling of lipid-protein interactions because the transmembrane region of the channel does not move much during unrestrained simulations. We compared the dynamics of the protein in the HMMM simulations with the ones in normal membranes without restraint. The transmembrane region is stable and does not move much for either simulation (average heavy atom RMSD was 1.57 Å for HMMM vs 2.00 Å for full-length). The RMSD for the transmembrane region in full-length membranes over the measured time scale (600 ns) is only ~0.43 Å larger than the HMMM simulations (500 ns). In comparison, the average heavy atom RMSD for the entire protein is 7.01 Å for HMMM simulations and 8.67 Å for full-length simulations, meaning

that most of the flexibility of the protein originates from the dynamics of the cytoplasmic and extracellular domains. Based on this observation, we conclude that the slight restraint on the protein will not affect results of the simulations.

Full-length Simulations. To investigate protein conformational changes upon PI(4,5)P_2 binding, the PI(4,5)P_2-bound HMMM systems were converted back to full-length phospholipids, followed by an additional 600-ns simulation without any restraints on the protein. A control simulation in the absence of PI(4,5)P_2 molecules was also performed using the same protocol.

Analysis of Lipid-protein Interactions. To characterize the interaction of lipid headgroups with potential binding sites on the protein, occupancy maps of the inositol group (and its phosphate groups) over the trajectories were calculated using the Volmap plugin in VMD (68). To determine the residues at those sites that stabilize PI(4,5)P_2 binding, the polar interactions between the residues (side-chain nitrogen/oxygen atoms) and the PI(4,5)P_2 inositol ring (phosphate/hydroxyl groups) in the binding site were calculated for each frame of the trajectory using a distance cutoff of 4 Å for phosphorus atoms of the phosphates and 3.5 Å for oxygen atoms of the hydroxyls.

Statistical Analysis. Data were analyzed using Origin 2017 SR2. Error bars are standard error of the mean. Statistics are described in each figure.

Data Sharing. All data presented in this paper will be made available to investigators upon reasonable request.

Acknowledgements

Research reported in this publication was supported by the National Eye Institute, National Institute of Arthritis and Musculoskeletal Diseases, and National Institute of General Medical Sciences of the National Institutes of Health under award numbers R01EY114852 (to HCH), R01AR067786 (to HCH), P41-GM104601 (to ET), and R01-GM123455 (to ET). 95% of this research was financed with Federal money and 5% from non-governmental sources. The content is solely the responsibility of the authors and does not necessarily represent the official views of the National Institutes of Health. We also acknowledge computing resources provided by Blue Waters at National Center for Supercomputing Applications, and Extreme Science and Engineering Discovery Environment (grant MCA06N060 to ET).

References

1. Hartzell C, Putzier I, & Arreola J (2005) Calcium-activated chloride channels. *Annu.Rev.Physiol* 67:719-758.
2. Fromm J & Lautner S (2007) Electrical signals and their physiological significance in plants. *Plant Cell Environ* 30(3):249-257.

3. Wozniak KL, Phelps WA, Tembo M, Lee MT, & Carlson AE (2018) The TMEM16A channel mediates the fast polyspermy block in Xenopus laevis. *J Gen Physiol* 150(9):1249-1259.
4. Pedemonte N & Galietta LJ (2014) Structure and Function of TMEM16 Proteins (Anoctamins). *Physiol Rev* 94(2):419-459.
5. Duvvuri U*, et al.* (2012) TMEM16A induces MAPK and contributes directly to tumorigenesis and cancer progression. *Cancer Res* 72(13):3270-3281.
6. Frings S, Reuter D, & Kleene SJ (2000) Neuronal Ca 2+ -activated Cl - channels--homing in on an elusive channel species. *Progress in Neurobiology* 60(3):247-289.
7. Malysz J*, et al.* (2017) Conditional genetic deletion of Ano1 in interstitial cells of Cajal impairs Ca(2+) transients and slow waves in adult mouse small intestine. *Am J Physiol Gastrointest Liver Physiol* 312(3):G228-G245.
8. Catalan MA*, et al.* (2015) A fluid secretion pathway unmasked by acinar-specific Tmem16A gene ablation in the adult mouse salivary gland. *Proc Natl Acad Sci U S A* 112(7):2263-2268.
9. Duran C & Hartzell HC (2011) Physiological roles and diseases of TMEM16/anoctamin proteins: are they all chloride channels? *Acta Pharmacol Sin* 32(6):685-692.
10. Bill A & Alex Gaither L (2017) The Mechanistic Role of the Calcium-Activated Chloride Channel ANO1 in Tumor Growth and Signaling. *Adv Exp Med Biol* 966:1-14.
11. Oh U & Jung J (2016) Cellular functions of TMEM16/anoctamin. *Pflugers Arch* 468(3):443-453.
12. Berg J, Yang H, & Jan LY (2012) Ca2+-activated Cl- channels at a glance. *J Cell Sci* 125(Pt 6):1367-1371.
13. Crottes D*, et al.* (2019) TMEM16A controls EGF-induced calcium signaling implicated in pancreatic cancer prognosis. *Proc Natl Acad Sci U S A* 116(26):13026-13035.
14. Schroeder BC, Cheng T, Jan YN, & Jan LY (2008) Expression Cloning of TMEM16A as a Calcium-Activated Chloride Channel Subunit. *Cell* 134:1019-1029.
15. Caputo A*, et al.* (2008) TMEM16A, A Membrane Protein Associated With Calcium-Dependent Chloride Channel Activity. *Science* 322:590-594.
16. Yang YD*, et al.* (2008) TMEM16A confers receptor-activated calcium-dependent chloride conductance. *Nature* 455:1210-1215.
17. Concepcion AR & Feske S (2017) Regulation of epithelial ion transport in exocrine glands by store-operated Ca(2+) entry. *Cell Calcium* 63:53-59.
18. Romanenko VG*, et al.* (2010) Tmem16A encodes the Ca^{2+}-activated Cl^- channel in mouse submandibular salivary gland acinar cells. *J Biol Chem* 285(17):12990-13001.
19. Ambudkar IS, Ong HL, Liu X, Bandyopadhyay BC, & Cheng KT (2007) TRPC1: the link between functionally distinct store-operated calcium channels. *Cell Calcium* 42(2):213-223.

20. Sung TS*, et al.* (2018) The cells and conductance mediating cholinergic neurotransmission in the murine proximal stomach. *J Physiol* 596(9):1549-1574.
21. Yu K, Zhu J, Qu Z, Cui YY, & Hartzell HC (2014) Activation of the Ano1 (TMEM16A) chloride channel by calcium is not mediated by calmodulin. *J Gen Physiol* 143(2):253-267.
22. Paulino C*, et al.* (2017) Structural basis for anion conduction in the calcium-activated chloride channel TMEM16A. *eLife* 6.
23. Dang S*, et al.* (2017) Cryo-EM structures of the TMEM16A calcium-activated chloride channel. *Nature* 552(7685):426-429.
24. Yu K, Duran C, Qu Z, Cui YY, & Hartzell HC (2012) Explaining calcium-dependent gating of anoctamin-1 chloride channels requires a revised topology. *Circ Res* 110(7):990-999.
25. Tien J*, et al.* (2014) A comprehensive search for calcium binding sites critical for TMEM16A calcium-activated chloride channel activity. *eLife* 3.
26. Terashima H, Picollo A, & Accardi A (2013) Purified TMEM16A is sufficient to form Ca2+-activated Cl- channels. *Proceedings of the National Academy of Sciences of the United States of America* 110(48):19354-19359.
27. Lim NK, Lam AK, & Dutzler R (2016) Independent activation of ion conduction pores in the double-barreled calcium-activated chloride channel TMEM16A. *J Gen Physiol* 148(5):375-392.
28. Jeng G, Aggarwal M, Yu WP, & Chen TY (2016) Independent activation of distinct pores in dimeric TMEM16A channels. *J Gen Physiol* 148(5):393-404.
29. Paulino C, Kalienkova V, Lam AKM, Neldner Y, & Dutzler R (2017) Activation mechanism of the calcium-activated chloride channel TMEM16A revealed by cryo-EM. *Nature* 552(7685):421-425.
30. Peters CJ*, et al.* (2018) The Sixth Transmembrane Segment Is a Major Gating Component of the TMEM16A Calcium-Activated Chloride Channel. *Neuron* 97(5):1063-1077 e1064.
31. Tian Y*, et al.* (2013) Control of TMEM16A by INO-4995 and other inositolphosphates. *Br J Pharmacol* 168(1):253-265.
32. De Jesus-Perez JJ*, et al.* (2017) Phosphatidylinositol 4,5-bisphosphate, cholesterol, and fatty acids modulate the calcium-activated chloride channel TMEM16A (ANO1). *Biochim Biophys Acta* 1863(3):299-312.
33. Ta CM, Acheson KE, Rorsman NJG, Jongkind RC, & Tammaro P (2017) Contrasting effects of phosphatidylinositol 4,5-bisphosphate on cloned TMEM16A and TMEM16B channels. *Br J Pharmacol* 174(18):2984-2999.
34. Pritchard HA, Leblanc N, Albert AP, & Greenwood IA (2014) Inhibitory role of phosphatidylinositol 4,5-bisphosphate on TMEM16A-encoded calcium-activated chloride channels in rat pulmonary artery. *Br J Pharmacol* 171(18):4311-4321.

35. Tembo M, Wozniak KL, Bainbridge RE, & Carlson AE (2019) Phosphatidylinositol 4,5-bisphosphate (PIP2) and Ca(2+) are both required to open the Cl(-) channel TMEM16A. *J Biol Chem*.
36. Suh BC & Hille B (2008) PIP2 is a necessary cofactor for ion channel function: how and why? *Annual review of biophysics* 37:175-195.
37. Hansen SB (2015) Lipid agonism: The PIP2 paradigm of ligand-gated ion channels. *Biochim Biophys Acta* 1851(5):620-628.
38. Logothetis DE*, et al.* (2015) Phosphoinositide control of membrane protein function: a frontier led by studies on ion channels. *Annu Rev Physiol* 77:81-104.
39. Jian X*, et al.* (2015) Molecular Basis for Cooperative Binding of Anionic Phospholipids to the PH Domain of the Arf GAP ASAP1. *Structure* 23(11):1977-1988.
40. Ford MG*, et al.* (2001) Simultaneous binding of PtdIns(4,5)P2 and clathrin by AP180 in the nucleation of clathrin lattices on membranes. *Science* 291(5506):1051-1055.
41. Hille B, Dickson EJ, Kruse M, Vivas O, & Suh BC (2015) Phosphoinositides regulate ion channels. *Biochim Biophys Acta* 1851(6):844-856.
42. Hansen SB, Tao X, & MacKinnon R (2011) Structural basis of PIP2 activation of the classical inward rectifier K+ channel Kir2.2. *Nature* 477(7365):495-498.
43. Wang W, Whorton MR, & MacKinnon R (2014) Quantitative analysis of mammalian GIRK2 channel regulation by G proteins, the signaling lipid PIP2 and Na+ in a reconstituted system. *eLife* 3:e03671.
44. Whorton MR & MacKinnon R (2011) Crystal structure of the mammalian GIRK2 K+ channel and gating regulation by G proteins, PIP2, and sodium. *Cell* 147(1):199-208.
45. Suh BC & Hille B (2007) Electrostatic interaction of internal Mg2+ with membrane PIP2 Seen with KCNQ K+ channels. *J Gen Physiol* 130(3):241-256.
46. Xiao Q*, et al.* (2011) Voltage- and calcium-dependent gating of TMEM16A/Ano1 chloride channels are physically coupled by the first intracellular loop. *Proc. Natl. Acad. Sci.* 108(21):8891-8896.
47. De Craene JO, Bertazzi DL, Bar S, & Friant S (2017) Phosphoinositides, Major Actors in Membrane Trafficking and Lipid Signaling Pathways. *Int J Mol Sci* 18(3).
48. Riehle RD, Cornea S, & Degterev A (2013) Role of phosphatidylinositol 3,4,5-trisphosphate in cell signaling. *Adv Exp Med Biol* 991:105-139.
49. Cabanos C, Wang M, Han X, & Hansen SB (2017) A Soluble Fluorescent Binding Assay Reveals PIP2 Antagonism of TREK-1 Channels. *Cell Rep* 20(6):1287-1294.
50. Li Y*, et al.* (2011) KCNE1 enhances phosphatidylinositol 4,5-bisphosphate (PIP2) sensitivity of IKs to modulate channel activity. *Proc Natl Acad Sci U S A* 108(22):9095-9100.
51. Lopes CM*, et al.* (2002) Alterations in conserved Kir channel-PIP2 interactions underlie channelopathies. *Neuron* 34(6):933-944.

52. Rosenhouse-Dantsker A & Logothetis DE (2007) Molecular characteristics of phosphoinositide binding. *Pflugers Arch* 455(1):45-53.
53. Brzeska H, Guag J, Remmert K, Chacko S, & Korn ED (2010) An experimentally based computer search identifies unstructured membrane-binding sites in proteins: application to class I myosins, PAKS, and CARMIL. *J Biol Chem* 285(8):5738-5747.
54. Aoun J*, et al.* (2016) Anoctamin 6 Contributes to Cl- Secretion in Accessory Cholera Enterotoxin (Ace)-stimulated Diarrhea: AN ESSENTIAL ROLE FOR PHOSPHATIDYLINOSITOL 4,5-BISPHOSPHATE (PIP2) SIGNALING IN CHOLERA. *J Biol Chem* 291(52):26816-26836.
55. Ye W*, et al.* (2018) Phosphatidylinositol-(4, 5)-bisphosphate regulates calcium gating of small-conductance cation channel TMEM16F. *Proc Natl Acad Sci U S A* 115(7):E1667-E1674.
56. Vermaas JV, Pogorelov TV, & Tajkhorshid E (2017) Extension of the Highly Mobile Membrane Mimetic to Transmembrane Systems through Customized in Silico Solvents. *The journal of physical chemistry. B* 121(15):3764-3776.
57. Baylon JL*, et al.* (2016) Atomic-level description of protein-lipid interactions using an accelerated membrane model. *Biochim Biophys Acta* 1858(7 Pt B):1573-1583.
58. Qi Y*, et al.* (2015) CHARMM-GUI HMMM Builder for Membrane Simulations with the Highly Mobile Membrane-Mimetic Model. *Biophys J* 109(10):2012-2022.
59. Vermaas JV*, et al.* (2015) Efficient Exploration of Membrane-Associated Phenomena at Atomic Resolution. *J Membr Biol* 248(3):563-582.
60. Pogorelov TV, Vermaas JV, Arcario MJ, & Tajkhorshid E (2014) Partitioning of amino acids into a model membrane: capturing the interface. *The journal of physical chemistry. B* 118(6):1481-1492.
61. Ohkubo YZ, Pogorelov TV, Arcario MJ, Christensen GA, & Tajkhorshid E (2012) Accelerating membrane insertion of peripheral proteins with a novel membrane mimetic model. *Biophys J* 102(9):2130-2139.
62. Tietjen GT*, et al.* (2017) Coupling X-Ray Reflectivity and In Silico Binding to Yield Dynamics of Membrane Recognition by Tim1. *Biophys J* 113(7):1505-1519.
63. Muller MP, Wang Y, Morrissey JH, & Tajkhorshid E (2017) Lipid specificity of the membrane binding domain of coagulation factor X. *J Thromb Haemost* 15(10):2005-2016.
64. Vermaas JV & Tajkhorshid E (2017) Differential Membrane Binding Mechanics of Synaptotagmin Isoforms Observed in Atomic Detail. *Biochemistry* 56(1):281-293.
65. Karandur D, Nawrotek A, Kuriyan J, & Cherfils J (2017) Multiple interactions between an Arf/GEF complex and charged lipids determine activation kinetics on the membrane. *Proc Natl Acad Sci U S A* 114(43):11416-11421.

66. Morales-Lazaro SL, Lemus L, & Rosenbaum T (2017) Regulation of thermoTRPs by lipids. *Temperature (Austin)* 4(1):24-40.
67. Rohacs T (2015) Phosphoinositide regulation of TRPV1 revisited. *Pflugers Arch* 467(9):1851-1869.
68. Delgado-Ramirez M, Lopez-Izquierdo A, & Rodriguez-Menchaca AA (2018) Dual regulation of hEAG1 channels by phosphatidylinositol 4,5-bisphosphate. *Biochem Biophys Res Commun* 503(4):2531-2535.
69. Lee SJ*, et al.* (2013) Secondary anionic phospholipid binding site and gating mechanism in Kir2.1 inward rectifier channels. *Nature communications* 4:2786.
70. D'Avanzo N, Lee SJ, Cheng WW, & Nichols CG (2013) Energetics and location of phosphoinositide binding in human Kir2.1 channels. *J Biol Chem* 288(23):16726-16737.
71. Campbell RB, Liu F, & Ross AH (2003) Allosteric activation of PTEN phosphatase by phosphatidylinositol 4,5-bisphosphate. *J Biol Chem* 278(36):33617-33620.
72. Brunner JD, Schenck S, & Dutzler R (2016) Structural basis for phospholipid scrambling in the TMEM16 family. *Curr Opin Struct Biol* 39:61-70.
73. Hildebrand PW*, et al.* (2009) SuperLooper--a prediction server for the modeling of loops in globular and membrane proteins. *Nucleic Acids Res* 37(Web Server issue):W571-574.
74. Olsson MH, Sondergaard CR, Rostkowski M, & Jensen JH (2011) PROPKA3: Consistent Treatment of Internal and Surface Residues in Empirical pKa Predictions. *J Chem Theory Comput* 7(2):525-537.
75. Rostkowski M, Olsson MH, Sondergaard CR, & Jensen JH (2011) Graphical analysis of pH-dependent properties of proteins predicted using PROPKA. *BMC Struct Biol* 11:6.
76. Humphrey W, Dalke A, & Schulten K (1996) VMD: visual molecular dynamics. *J Mol Graph* 14(1):33-38, 27-38.
77. Zhang L & Hermans J (1996) Hydrophilicity of cavities in proteins. *Proteins* 24(4):433-438.
78. Morozenko A, Leontyev IV, & Stuchebrukhov AA (2014) Dipole Moment and Binding Energy of Water in Proteins from Crystallographic Analysis. *J Chem Theory Comput* 10(10):4618-4623.
79. Wu EL*, et al.* (2014) CHARMM-GUI Membrane Builder toward realistic biological membrane simulations. *J Comput Chem* 35(27):1997-2004.
80. Jorgensen WL, Chandrasekhar J, Madura JD, Impey RW, & Klein ML (1983) Comparison of simple potential functions for simulating liquid water. *J. Chem. Phys.* 79:926-935.
81. Phillips JC*, et al.* (2005) Scalable molecular dynamics with NAMD. *J Comput Chem* 26(16):1781-1802.
82. Klauda JB*, et al.* (2010) Update of the CHARMM all-atom additive force field for lipids: validation on six lipid types. *The journal of physical chemistry. B* 114(23):7830-7843.

83. Darden T, York D, & Pedersen L (1998) Particle mesh Ewald: An N·log(N) method for Ewald sums in large systems. *J. Chem. Phys.* 98:10089-10092.
84. Nose S (1984) A unified formulation of the constant temperature molecular dynamics methods. *J. Chem. Phys.* 81:511-519.
85. Hoover WG (1985) Canonical dynamics: Equilibrium phase-space distributions. *Phys Rev A Gen Phys* 31(3):1695-1697.
86. Smart OS, Neduvelil JG, Wang X, Wallace BA, & Sansom MS (1996) HOLE: a program for the analysis of the pore dimensions of ion channel structural models. *J Mol Graph* 14(6):354-360, 376.

	MD Simulation	**PI(4,5)P_2 Effect**
	Probability	Mutant/WT X100
SITE A/1		
R433	0.52	36
K430	0.47	4
R429	0.18	-5
R437	0.17	0
K313	0.07	-8
SITE B/2		
K668	0.29	42
R665	0.22	23
R670	0.15	46
K659	0.15	44
K662	0.13	20
R677	0.12	60
K740	0.06	84
R683	0.06	-2
K661	0.05	86
K682	-	6
K684	-	1
SITE C/4		
R484	0.35	48
R461	0.31	10
K465	0.25	106
K480	0.23	0
R468	0.20	100
R472	0.14	100
OTHERS		
R125	N-terminus	4
R579	Structural ?	-1
R747	Structural ?	12

Table I. Comparison of amino acids in PI(4,5)P_2 sites identified by MD simulation and mutagenesis. MD probability is probability of the amino acid coordinating PI(4,5)P_2 within that site (Fig. 7). PI(4,5)P_2 effect is expressed as % of effect on wild type ANO1.